Available online at www.sciencedirect.com
ScienceDirect
Coordination Chemistry Reviews 251 (2007) 364–378
COORDINATION CHEMISTRY REVIEWS
www.elsevier.com/locate/ccr

Review

Spin-crossover in cobalt(II) imine complexes

Itana Krivokapic [a], Mohamed Zerara [a], Max Lawson Daku [a], Alfredo Vargas [a], Cristian Enachescu [b], Christina Ambrus [c], Philip Tregenna-Piggott [d], Nahid Amstutz [a], Elmars Krausz [e], Andreas Hauser [a,*]

[a] *Département de chimie physique, Université de Genève, Bâtiment de Science 2, 30 quai Ernest-Ansermet, CH-1211 Genève 4, Switzerland*
[b] *Department of Solid State and Theoretical Physics, "Alexandru Ioan Cuza" University, 11 Blvd. Carol, R-700506 Iasi, Romania*
[c] *Departement für Chemie und Biochemie, Universität Bern, Freiestrasse 3, CH-3000 Bern 9, Switzerland*
[d] *Laboratory for Neutron Scattering, ETHZ and Paul-Scherrer, Institute, CH-5232 Villigen PSI, Switzerland*
[e] *Research School of Chemistry, Australian National University Building 35, Science Rd., Canberra ACT 0200, Australia*

Received 28 February 2006; accepted 12 May 2006
Available online 19 May 2006

Contents

Abstract

Whereas there are hundreds of known iron(II) spin-crossover compounds, only a handful of cobalt(II) spin-crossover compounds have been discovered to date, and hardly an in depth study on any of them exists. This review begins with an introduction into the theoretical aspects to be considered when discussing spin-crossover compounds in general and cobalt(II) systems in particular. It is followed by case studies on $[Co(bpy)_3]^{2+}$ and $[Co(terpy)_2]^{2+}$ (bpy = 2,2′-bipyridine, terpy = 2,2′:6′,2″-terpyridine) presenting and discussing results from magnetic susceptibility measurements, X-ray crystallography, optical spectroscopy, and EPR spectroscopy.

Keywords: Spin-crossover; Cobalt(II)-tris-2,2′-bipyridine; Cobalt(II)-bis-2,2′:6′,2″-terpyridine; Ligand-field theory; Density functional theory

* Corresponding author. Tel.: +41 22 379 6559; fax: +41 22 379 6103.
E-mail address: andreas.hauser@unige.ch (A. Hauser).

0010-8545/$ – see front matter © 2006 Elsevier B.V. All rights reserved.
doi:10.1016/j.ccr.2006.05.006

1. Introduction

Spin-crossover complexes of transition metal ions having a d^4–d^7 electronic configuration are characterised by two low-lying electronic states of different spin-multiplicities: the low-spin (LS) state with a maximum number of paired electrons in the t_{2g} subshell as the electronic ground state, and the high-spin (HS) state with the electrons entering the d-orbitals according to Hund's rule as thermally accessible state at comparatively low temperatures. The phenomenon of spin-crossover was discovered by Cambi et al. on a series of iron(III) tris-dithiocarbamate compounds more than 70 years ago [1]. In octahedral symmetry, the two states involved are the $^2T_2(t_{2g}^5)$ state as low-spin state and the $^6A_1(t_{2g}^3e_g^2)$ state as high-spin state. The first cobalt(II) compound to show spin-crossover, namely $[Co(L)_2]X_2$, where L = a tridentante terimine ligand, was presented by Stoufer et al. [2] in 1961, the spin transition occurring between the $^2E(t_{2g}^6e_g^1)$ and the $^4T_1(t_{2g}^5e_g^2)$ state. This was followed by the discovery of spin-crossover from the low-spin $^1A_1(t_{2g}^6)$ state to the high-spin $^5T_2(t_{2g}^4e_g^2)$ state in the iron(II) compound $[Fe(phen)_2(SCN)_2]$ by Madeja and König [3] in 1963.

The thermal spin transition is entropy driven and occurs from the low-spin state at low temperatures to an almost quantitative population of the high-spin state at elevated temperatures. In dilute systems, that is, in liquid or rigid solutions as well as in doped crystalline materials, the thermal spin transition is gradual corresponding to a Boltzmann distribution between the two vibronic manifolds. The temperature at which the fraction of complexes in the high-spin state $\gamma_{HS} = \frac{1}{2}$, generally referred to as the transition temperature $T_{1/2}$, is a measure for the difference in zero-point energy $\Delta E^{\circ}_{HL} = E^{\circ}_{HS} - E^{\circ}_{LS}$ between the two states. In neat spin-crossover compounds, transition curves tend to be more abrupt and may occur as first order phase transitions with a hysteresis. Such a cooperative behaviour is due to elastic interactions [4] between the spin-crossover complexes, which result from the comparatively large differences in molecular geometry between the two states. For iron(II) complexes it is essentially the metal–ligand bond lengths which are most affected by the spin transition, with typical values of the bond-length difference $\Delta r_{HL} = r_{HS} - r_{LS} \approx 0.18$–$0.2$ Å [5] due to the transfer of two electrons to the anti-bonding e_g orbitals and concurrent loss of π back bonding from the t_{2g} orbitals. For iron(III) spin-crossover systems π back bonding is of lesser importance and therefore the average bond length difference is with 0.13–0.16 Å somewhat smaller [6]. For cobalt(II) complexes only one electron is transferred to the anti-bonding orbital upon spin-crossover, as a consequence the average bond-length difference is only 0.07 to 0.11 Å [7,8]. In addition, the $^2E(t_{2g}^6e_g^1)$ low-spin state is susceptible to a Jahn–Teller effect [9].

Over the past two decades spin-crossover compounds have been intensively investigated by an ever-larger number of research groups, as borne out in particular by the recent volumes of "Topics in Current Chemistry" exclusively dedicated to this phenomenon [10]. The majority of known spin-crossover complexes today have iron(II) as central metal ion, and several in depth studies on a number of iron(II) complexes addressing many different aspects of spin-crossover have been published.

The number of known cobalt(II) spin-crossover complexes is comparatively small, and essentially only two reviews [11,12] discuss cobalt(II) spin-crossover complexes in any detail. We begin the present article with a brief discussion of the relevant literature on cobalt(II) spin-crossover complexes. This is followed by some theoretical considerations basically within the framework of ligand-field theory. The case studies on $[Co(bpy)_3]^{2+}$ and $[Co(terpy)_2]^{2+}$ (bpy = 2,2′-bipyridine, terpy = 2,2′:6′,2″-terpyridine) constitute the main body of the article.

The chief experimental methods used for studying spin-crossover compounds are magnetic susceptibility measurements to characterise the spin state, and X-ray diffraction and EXAFS for structural properties. Unfortunately one of the most useful techniques for iron(II) spin-crossover systems, namely Mössbauer spectroscopy, is not available for cobalt(II) complexes. On the other hand, EPR spectroscopy is quite useful. Even though it does not allow to follow the spin transition quantitatively, it gives information on the local symmetry, multiplet splittings and Jahn–Teller distortions. Furthermore, useful information on the ligand-field strength and the nature of higher lying excited states can be obtained by optical spectroscopy.

2. A short review of the relevant literature

The coordination motif of the first cobalt(II) complex with the tri-dentate terimine ligand [2] found to exhibit spin-crossover constitutes the basic motif for a whole class of cobalt(II) spin-crossover compounds. The most prominent member is the $[Co(terpy)_2]^{2+}$ complex in combination with a number of different anions [13]. The coordination motif of two tri-dentate ligands seems particularly suited to stabilise the low-spin state, as it is predisposed to allow for anisotropic bond length changes. In the low-spin state the axial bond length is 1.912 Å, whereas the equatorial bond length is 2.083 Å [14]. The short axial bond length in the low-spin state destabilises the d_{z^2} orbital, which, in turn, stabilises one of the component of the ^2E low-spin state. The concomitant elongation of the equatorial metal–ligand bond length is a manifestation of the Jahn–Teller effect [9]. In the high-spin state the axial Co–N bond length has been estimated to be 0.21 Å larger than in the low-spin state, whereas the equatorial bond length difference is only 0.08 Å [14]. Thus, in the high-spin state the coordination octahedron is much less distorted than in the low-spin state. Subsequently a number of spin-crossover complexes based on ligands with coordination motif of terpy have been described in the literature, for instance, the closely related compound with terpyridone as ligand [15], but also more complex and even polynuclear structures [16].

Even though bpy is generally considered a stronger ligand than terpy, the $[Co(bpy)_3]^{2+}$ is usually a classic high-spin complex [17]. This supports the statement that the anisotropic bond length change in the terpy complex actively stabilises the low-spin state via a reinforced Jahn–Teller effect. However, even the $[Co(bpy)_3]^{2+}$ complex can be turned into spin-crossover complex when it is confined to the cavities of Zeolites [18] or

embedded into a three-dimensional oxalate network [8]. In the Zeolites the thermal spin transition is very gradual, and at room temperature the high-spin fraction is still less than 50%. In the oxalate network the transition is considerably steeper, indicating that cooperative effects are not negligible [19]. In the latter, single crystal X-ray crystallography gave a value of $\Delta r_{HL} = 0.1$ Å, with no indication of a symmetry lowering in the low-spin state. Thus in a first approximation the effect of the confining environment may be regarded as "chemical pressure" destabilising the high-spin state sufficiently for the low-spin state to become the electronic ground state. However, as X-ray crystallography only gives an average geometry, dynamic distortions cannot be ruled out. Other tris diimine spin-crossover complexes were obtained through a chemical increase in ligand-field strength as compared to bpy by attaching electron rich substituents on the imine groups [20].

Another class of octahedral cobalt(II) spin-crossover complexes is provided by Schiff base ligands with $[CoN_4O_2]$ coordination [21]. They mostly show very abrupt spin transitions, which are triggered by first order crystallographic phase transitions. Based on EXAFS spectroscopy, the average metal–ligand bond length difference was estimated to be ~0.1 Å, with a substantially larger difference of the Co–N bond length than for the Co–O bond length. At present a cooperative Jahn–Teller effect is thought to be responsible for the observed behaviour. In addition a number of five-coordinate cobalt(II) spin-crossover complexes have been investigated [22]. For a complete review of the literature on cobalt(II) spin-crossover complexes the reader is referred to the recent and very thorough text by Goodwin [12].

3. Theoretical background

3.1. Ligand-field theory

Fig. 1 shows the Tanabe–Sugano diagram for an octahedral d^7 system using the Racah parameters of electron-electron repulsion appropriate for cobalt(II) [23]. In a weak ligand field the high-spin $^4T_1(t_{2g}^5e_g^2)$ state is the electronic ground state, in a strong ligand field it is the low-spin $^2E(t_{2g}^6e_g^1)$ state. From a ligand-field theoretical point of view, the phenomenon of spin-crossover is due to the fact that the ligand-field strength for a given metal ligand combination decreases with increasing metal–ligand bond length as r^{-n}, $n = 5$–6, whereas the electron–electron repulsion decreases only indirectly via a small decrease in the nephelauxetic effect [24]. Thus, as upon spin-crossover and promotion of one electron from the non-bonding t_{2g} orbital to the anti-bonding e_g orbital the bond length changes, the ligand-field strength changes likewise. Fig. 2 shows the configurational coordinate diagram for the two low-lying spin states along the metal–ligand bond length, that is along the totally symmetric breathing mode. At the potential minimum of the low-spin state, the ligand-field strength is on the strong-field side of the crossover point in the Tanabe–Sugano diagram, and at the potential minimum of the high-spin state it is on the weak-field side as indicated in Fig. 1. The energies of the respective excited states in the Tanabe–Sugano diagram correspond to the vertical Franck–Condon energies in the configurational coordinate diagram.

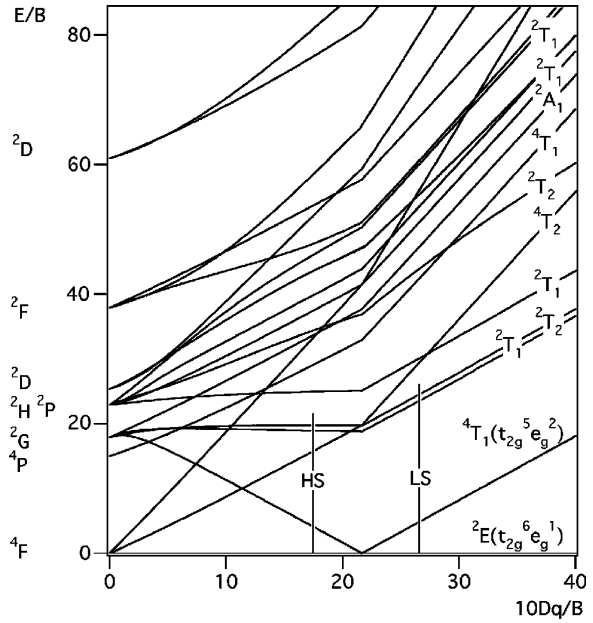

Fig. 1. Tanabe–Sugano diagram for an octahedral cobalt(II) complex, calculated with $C/B = 4.63$. For the free cobalt(II) ion $B = 971\ cm^{-1}$ and $C = 4496\ cm^{-1}$ [23]. In the complex B and C are usually reduced by an orbital reduction factor β.

The $\Delta S = 0$ spin-selection rule for optical transitions predicts very different optical properties for the two spin states. Whereas for the high-spin species essentially one spin-allowed transition corresponding to the $^4T_1(t_{2g}^5e_g^2) \rightarrow {}^4T_2(t_{2g}^4e_g^3)$ transition in the near infrared is expected, several such transitions in the visible are to be expected for the low-spin species, the lowest ones corre-

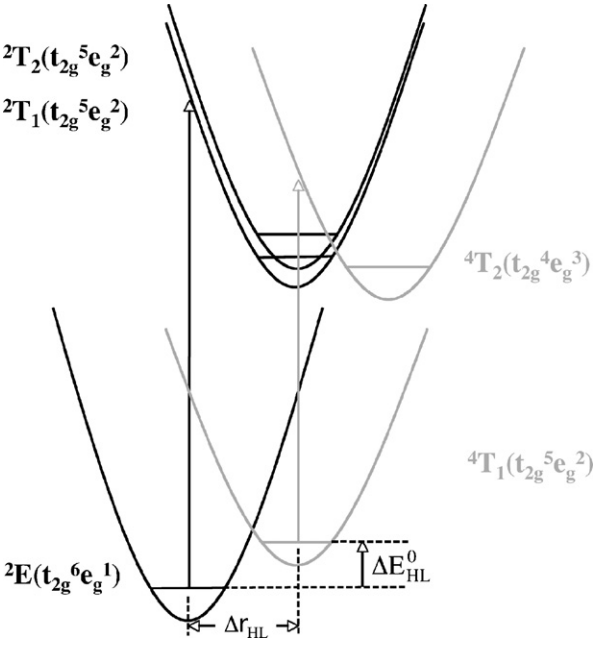

Fig. 2. Configurational coordinate diagram for a cobalt(II) spin-crossover system including the lowest excited states ligand-field states.

sponding to the $^2E(t_{2g}^6e_g^1) \rightarrow {}^2T_2(t_{2g}^5e_g^2)$, $^2T_1(t_{2g}^5e_g^2)$ transitions. In addition to the ligand-field transitions one may expect metal to ligand charge transfer (MLCT) transitions at comparatively low energies [17]. These are normally more intense and at lower energy for the low-spin species than for the high-spin species because of the shorter bond length and thus the better overlap between metal and ligand orbitals. Thus in addition to magnetic susceptibility measurements, optical spectroscopy may likewise serve to identify the spin state of a given complex and to follow, for instance, the spin transition as a function of temperature.

Of course, the most easily accessible quantity for the determination of the spin state of a given complex and for following a thermal spin transition is provided by the magnetic susceptibility. For the low-spin state, the product of the molar magnetic susceptibility and temperature, χT, takes on a value very close to the spin-only value of 0.375 $cm^3\ mol^{-1}$ K and is almost independent of the effective local geometry. For the high-spin state, χT is temperature dependent because of the orbital contribution, in particular for the comparatively high symmetry complexes considered here. Fig. 3a shows χT as a function of temperature for the $^4T_1$ state in octahedral symmetry calculated both in the weak-field and in the strong-field limits according to Mabbs and Machin [25]. As is well known, in a complex the Racah parameters B and C and the spin–orbit coupling constant ζ are reduced with respect to their free ion values by the so-called orbital reduction factor β. Thus in order to be as close to experiment as possible, the curves in Fig. 3 were calculated by setting $\beta = 0.75$. In addition, Fig. 3a shows the χT curve for an intermediate ligand-field strength of 10Dq = 12,000 cm^{-1}, corresponding to a factor $A = 1.4$ for the configuration mixing between the $^4T_1(t_{2g}^6e_g^2)$ and the $^4T_1(t_{2g}^4e_g^3)$ state according to Mabbs and Machin [25].

3.2. Symmetry lowering and the Jahn–Teller effect

The actual symmetry of most if not all spin-crossover complexes is considerably lower than O_h. More specifically, the complexes to be treated in detail below, that is $[Co(bpy)_3]^{2+}$ and $[Co(terpy)_2]^{2+}$, belong to the point groups D_3 and D_{2d}, respectively. For the former, the coordination octahedron is axially compressed along the trigonal axis, the latter essentially is compressed along the tetragonal axis, as in D_{2d} the S_4 axis is preserved. Fig. 4a schematically shows the orbital splittings for a trigonal and a tetragonal compression, and Fig. 4b shows the splittings of the high-spin and the low-spin state of the d^7 configuration according to point charge considerations. For a tetragonal compression this usually gives the correct sign, for a trigonal distortion with bis-chelating ligands this is often not the case because of the Orgel effect [26].

The first order splitting of the high-spin state is conveniently expressed by the splitting parameters Δ_{trig} and Δ_{tetr}, respectively. Fig. 5 shows the splitting of the $^4T_1$ state as function of the axial splitting parameter under the combined effects of the axial distortion and spin–orbit coupling. Such axial splittings influence the magnetic susceptibility as well as the EPR and the optical spectra. Fig. 3b shows χT, spatially averaged, as a function of temperature calculated for both trigonal and tetragonal

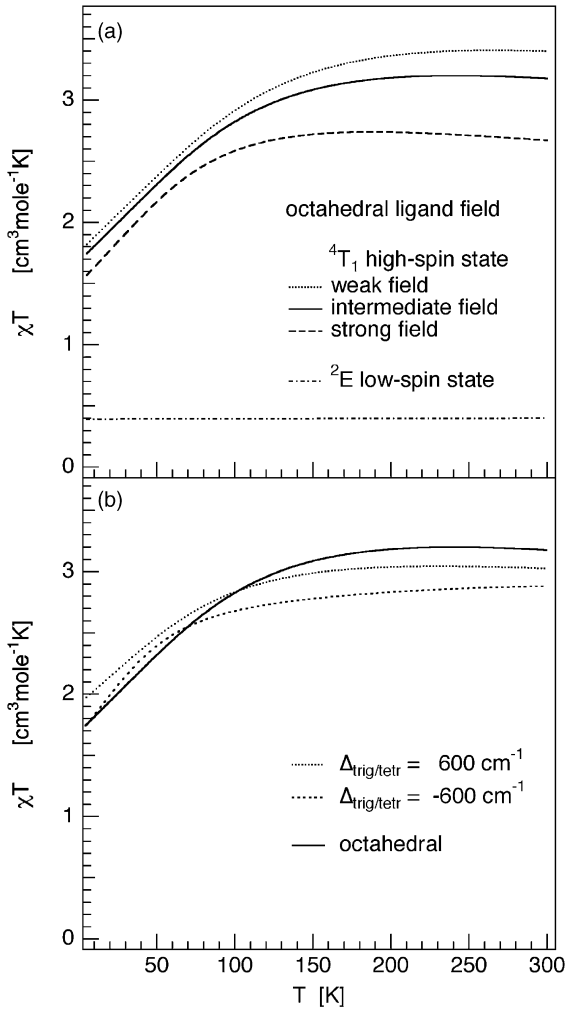

Fig. 3. The magnetic susceptibility of cobalt(II) plotted as χT vs. T calculated. (a) In octahedral symmetry for the high-spin state (···) weak-field limit, (- - -) strong-field limit, (—) intermediate field with 10Dq = 12,000 cm^{-1}, and for the low-spin state (-·-·-·-). All parameters are reduced by an orbital reduction factor $\beta = 0.75$ from their free ion values, $B = 700\ cm^{-1}$ (free ion value 971 cm^{-1} [23]), $C = 3250\ cm^{-1}$ (free ion value 4497 cm^{-1} [23]), $C/B = 4.63$, and $\zeta = 400\ cm^{-1}$ (free ion value 515 cm^{-1} [23]); (b) in an axially distorted complex, $\Delta_{trig/tetr} = +600\ cm^{-1}$ (···), $\Delta_{trig/tetr} = -600\ cm^{-1}$ (-·-·-·) with all other parameters set to the values of the intermediate field. The curve for octahedral symmetry is included for comparison.

splittings of $\Delta_{trig/tetr} = \pm 600\ cm^{-1}$ in comparison to the octahedral limit. The values for the other parameters, namely B, C, 10Dq and ζ, have been fixed at the values of the intermediate field with the orbital reduction factor $\beta = 0.75$. Fig. 6 shows $g_\parallel$ and $g_\perp$ of the lowest energy Kramers doublet of the $^4T_1$ manifold for both positive (compressed) and negative (elongated) values of Δ_{trig} and Δ_{tetr}, respectively.

For the ^2E low-spin state in octahedral symmetry the g-value of the two degenerate Kramers doublets is 2 to first order. Second order spin–orbit coupling to the $^4T_1$ state results in a value slightly above 2. A static tetragonal distortion results in a large first order splitting of the ^2E state as shown in Fig. 4b. The g-value of the lower energy component remains almost isotropic close to 2. For a compression of the octahedron, typically $g_\perp > g_\parallel > 2$. A static trigonal distortion, on the other hand,

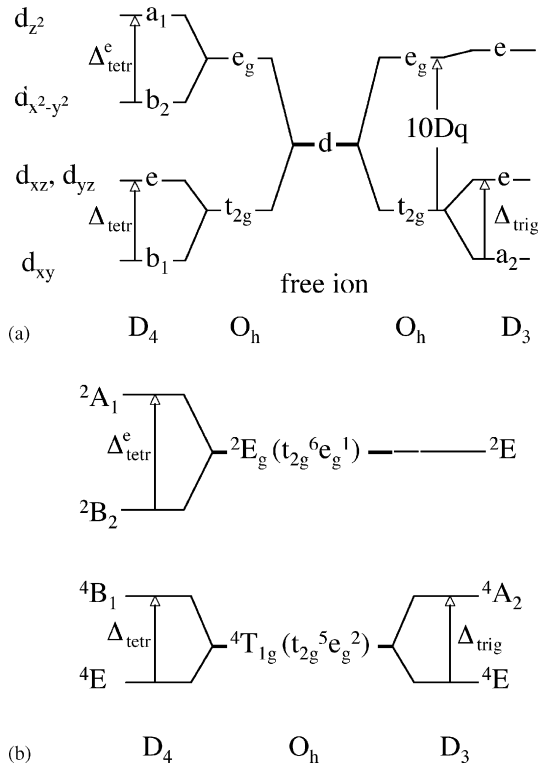

Fig. 4. (a) Splitting of the d orbitals in axially distorted pseudo-octahedral complexes. (b) Splitting of the two low-lying ligand field states of cobalt(II) d^7 in axially distorted pseudo-octahedral complexes. As shown, the energetic ordering of orbitals and states corresponds to a compressed octehedron according to a point charge model.

does not give a first order splitting of the octahedral ^{2}E state. However together with spin–orbit coupling it results in a zero-field splitting of the ^{2}E state of some tens of wavenumbers. The value for $g_\parallel$ for both Kramers doublets remains close to 2, however the value for $g_\perp$ approaches zero. This is not what is actually

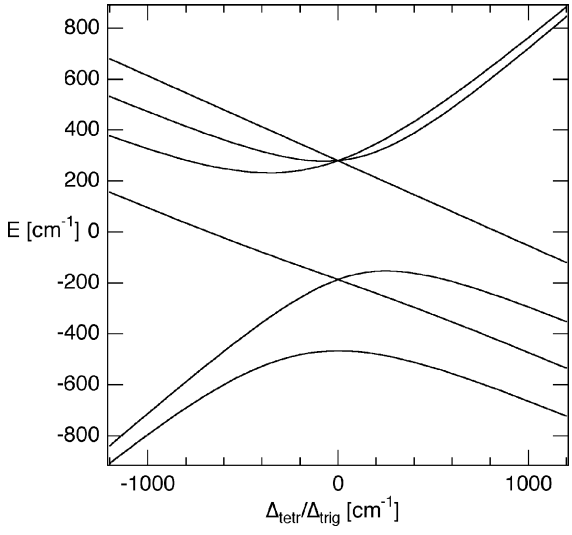

Fig. 5. Splitting of the ^{4}T$_1$ state into six Kramers doublets under the combined influence of an axial ligand field and spin–orbit coupling. Parameter values used for the calculation are the same as those used for the case of the intermediate field in Fig. 3b.

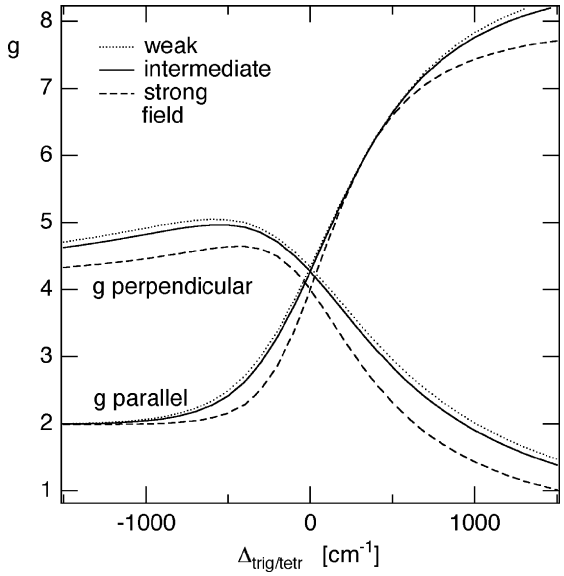

Fig. 6. Calculated g values of the lowest energy Kramers doublet of the ^{4}T$_1$ state as a function of the trigonal and the tetragonal splitting parameters Δ_{trig} and Δ_{tetr}, respectively.

observed (see below). As the ^{2}E state in trigonal symmetry contains an unpaired electron in the e_g orbitals, it is susceptible to an e × e Jahn–Teller effect with the typical warped Mexican hat potential [27]. Effectively, this overlays a static or a dynamic tetragonal distortion onto the D_3 symmetry as shown in Fig. 7, which, if dominant, once again results in an almost isotropic g-value close to 2.

In conclusion, ligand-field theory allows a qualitative or even semi-quantitative understanding of the physical properties of transition metal compounds. As described above, it explains in an easy to understand model how the phenomenon of spin-crossover comes about. However, it does not provide a quantitative description of structural changes, frequency shifts in the vibrational spectrum and energetic parameters. Today density functional theory (DFT) has become a standard computational technique for open shell systems [28], and it is known to perform extremely well with regard to structure optimisation and vibrational frequency calculations in spin-crossover systems [29]. With regard to energetic parameters, in the present case for instance the zero-point energy difference between the two spin states, the performance of modern functionals puts them into the right order of magnitude, but the precision is not yet sufficient to calculate them within the required hundred wavenumbers.

3.3. The thermodynamics of the spin transition in cobalt(II) complexes

The thermodynamic treatment of spin transitions of dilute systems is often performed by fitting the expression for the high-spin fraction

$$\gamma_{HS}(T) = \frac{e^{-\Delta G^\circ_{HL}}}{1 + e^{-\Delta G^\circ_{HL}}} \quad (1)$$

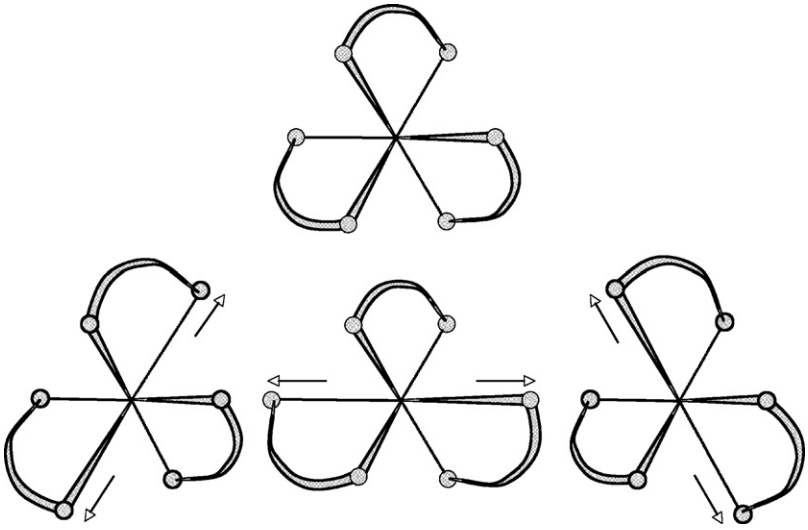

Fig. 7. Tetragonal Jahn–Teller distortion of the ^{2}E state in D_3 symmetry. The corresponding potential energy surface has the form of the famous warped Mexican hat.

to the experimental transition curve. In Eq. (1) the standard Gibbs free energy of reaction of the LS ↔ HS equilibrium is given by

$$\Delta G^{\circ}_{\mathrm{HL}} = \Delta H^{\circ}_{\mathrm{HL}} - T\Delta S^{\circ}_{\mathrm{HL}} \tag{2}$$

and in the fit procedure the standard enthalpy and the standard entropy of reaction are assumed to be independent of temperature within the interval of the spin transition. For iron(II) this procedure works quite well, except for systems with transition temperatures below 100 K. This is due to the fact that despite being gradual, the typical value of $\Delta S^{\circ}_{\mathrm{HL}}$ for iron(II) systems of around 5 $\mathrm{cm^{-1}\,K^{-1}}$ (60 $\mathrm{J\,mol^{-1}\,K^{-1}}$) ensures a comparatively narrow temperature interval for the spin transition. The fit values for $\Delta H^{\circ}_{\mathrm{HL}}$ and $\Delta S^{\circ}_{\mathrm{HL}}$ should then be interpreted as the values at the transition temperature

$$T_{1/2} = \frac{\Delta H^{\circ}_{\mathrm{HL}}}{\Delta S^{\circ}_{\mathrm{HL}}} \tag{3}$$

For other spin-crossover systems, this procedure can still be adopted, but it does not provide any information on the actual temperature dependence of $\Delta H^{\circ}_{\mathrm{HL}}$ and $\Delta S^{\circ}_{\mathrm{HL}}$. This dependence can be quite substantial [30]. In particular in the case of a small zero-point energy difference $\Delta E^{\circ}_{\mathrm{HL}}$ and comparatively small multiplet splittings this procedure is no longer really applicable.

Already at an early stage, Barraclough et al. [31] tried to model the thermal spin transition in cobalt(II) complexes based on a ligand-field model and statistical thermodynamics. They included spin–orbit coupling between the two spin states in their treatment, but at the time they were not aware of the large difference in metal–ligand bond length between the two states, and in their model calculations they took the zero-point energy difference to be equal to the vertical energy difference. In addition they ignored the important vibrational contribution to the entropy difference between the two spin states. A more realistic model takes into account both the specific multiplet splittings of the two states as well as the higher density of vibrational states in the high-spin state. For second order spin–orbit coupling between the two states, the vertical energy difference at the respective potential minima is the decisive quantity and not the zero-point energy difference. As these energy differences are quite large, second order spin–orbit coupling constitutes only a minor perturbation.

In the solid state but without considering interactions between spin-changing complexes and at ambient pressure the standard Gibbs free energy is almost equal to the standard free energy

$$\begin{aligned}\Delta G^{\circ}_{\mathrm{HL}} &= -k_{\mathrm{B}}T\ln\left(\frac{\gamma_{\mathrm{HS}}}{\gamma_{\mathrm{LS}}}\right) \approx \Delta F^{\circ}_{\mathrm{HL}} \\ &= \Delta E^{\circ}_{\mathrm{HL}} - k_{\mathrm{B}}T\ln\left(\frac{Z_{\mathrm{HS}}}{Z_{\mathrm{LS}}}\right)\end{aligned} \tag{4}$$

In Eq. (4), the zero-point energy difference is defined as the difference between the lowest energy components of the respective spin multiplets, Z_{HS} and Z_{LS} are the molecular partition functions in the high-spin and in the low-spin state, respectively. Assuming the total wave functions to be separable into products of electronic and vibrational wave functions, and assuming furthermore that for a given spin multiplet the vibrational frequencies are the same for all components, the molecular partition functions can be expressed as

$$Z_{\mathrm{IS}} = Z^{\mathrm{el}}_{\mathrm{IS}} Z^{\mathrm{vib}}_{\mathrm{IS}} = Z^{\mathrm{vib}}_{\mathrm{IS}} \sum_i g_i \mathrm{e}^{-\varepsilon_i/k_{\mathrm{B}}T} \tag{5}$$

In Eq. (5), IS = HS or LS, i sums over all electronic components of a given spin state, ε_i and g_i are the corresponding electronic energies and degeneracies, respectively, with the zero-point energy of the lowest component of each electronic state set to zero. The vibrational partition function

$$Z^{\mathrm{vib}}_{\mathrm{IS}} = \prod_k \frac{1}{1-\mathrm{e}^{\hbar\omega^{\mathrm{IS}}_k/k_{\mathrm{B}}T}} \approx \left(\frac{1}{1-\mathrm{e}^{\hbar\omega_{\mathrm{IS}}/k_{\mathrm{B}}T}}\right)^n \tag{6}$$

where k includes all normal modes of the complex and where the ω^{IS}_ks are the corresponding frequencies in the respective spin state. Assuming that the important frequency shifts between the

LS and the HS state are confined to the coordination polyhedron, the product in Eq. (6) can be approximated by restricting k to the 15 normal modes of the octahedron and by considering a mean active vibrational frequency ω_{IS} for each spin state. Typical values for such an average vibrational frequency are $\sim 100\,cm^{-1}$. For cobalt(II) the vibrational frequency shift between the two spin states is much smaller than for iron(II) spin-crossover compounds. It is not expected to be more than 15% for the metal ligand vibrations based on DFT frequency calculations [32]. Alternatively, such frequency calculations in the high-spin and the low-spin state can be used calculate the product in Eq. (6) exactly.

Because of the smaller metal–ligand bond length difference, cooperative effects in cobalt(II) spin-crossover compounds are usually not as important as in iron(II) systems, nevertheless they can by no means be neglected. In mean-field approximation the standard Gibbs free energy in a mixed crystal with the concentration x of the spin-crossover complex in an inert host lattice can be expressed by Eq. (7) according to Ref. [4].

$$\Delta G^{x}_{HL} = \Delta G^{\circ}_{HL} - 2x\Gamma_{int}\left(\gamma_{HS} - \frac{1}{2}\right) - \Delta_{lat}(1-x) \qquad (7)$$

In Eq. (7), ΔG°_{HL} is the standard Gibbs free energy in the absence of elastic interactions, for instance as determined in the dilute mixed crystal and corrected for a lattice shift Δ_{lat} taking into account a shift in ΔH°_{HL} when going from the dilute mixed crystal to the neat compound [4]. Γ_{int} is the interaction constant. ΔG°_{HL} can either be expressed by Eq. (2), with ΔH°_{HL} and ΔS°_{HL} as constants, or Eqs. (4)–(6) may be used, provided the electronic energies for the multiplet splittings and the vibrational frequencies are known, for instance from experiment or from computational studies. In the former the transition temperature is given by

$$T_{1/2} = \frac{\Delta H^{\circ}_{HL} - (1-x)\Delta_{lat}}{\Delta S^{\circ}_{HL}} \qquad (8)$$

Depending upon the sign of Δ_{lat}, the host lattice can either stabilise or destabilise the low-spin state. Based on the picture of a "chemical" pressure, for a confining host lattice $\Delta_{lat} < 0$, for a host lattice which provides large cavities for the guest $\Delta_{lat} > 0$. The interaction constant Γ_{int} is almost exclusively positive, that is, except for systems with very specific nearest neighbour interactions, cooperative effects favour the majority species, and result in steep transition curves.

4. Case studies

4.1. The cobalt(II)-tris-2,2′-bipyridine complex

In solution or as a simple salt with a number of different anions, and even when incorporated into the three-dimensional oxalate network of composition $[Co(bpy)_3][NaM(ox)_3]$ (M = Cr, Rh), the $[Co(bpy)_3]^{2+}$ complex has a high-spin $^4T_1$ ground state. But, as mentioned in the introduction, the effective ligand-field strength is quite close to the crossover point so that the low-spin ^2E state has to be at comparatively low energy. A small

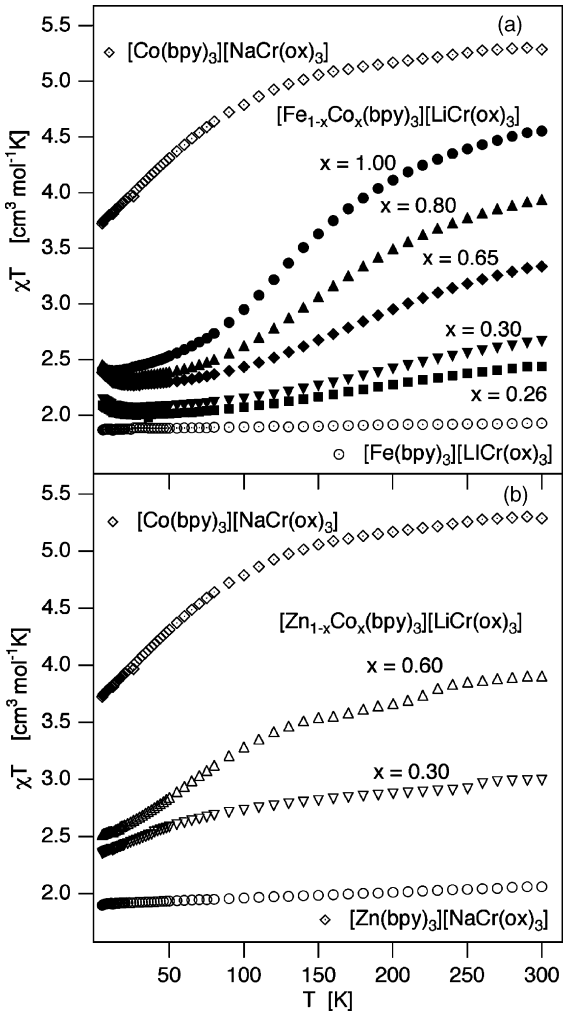

Fig. 8. Magnetic susceptibility of (a) neat $[Co(bpy)_3][NaCr(ox)_3]$, the $[Fe_{1-x}Co_x(bpy)_3][LiCr(ox)_3]$ mixed crystal series, and neat $[Fe(bpy)_3][NaCr(ox)_3]$ (adapted from Ref. [19a]), and (b) the $[Zn_{1-x}Co_x(bpy)_3][LiCr(ox)_3]$ mixed crystal series, and $[Zn(bpy)_3][NaCr(ox)_3]$, plotted as χT vs. T.

"chemical" pressure in the form a confining environment, for instance inside the cages of Zeolites or in the more tightly fitting cavity of the oxalate network with Li instead of Na, destabilises the high-spin state sufficiently for the low-spin state to become the ground state [8,19]. This is to be discussed in detail below.

4.1.1. Magnetic susceptibility

The powder magnetic susceptibility of $[Co(bpy)_3][NaCr(ox)_3]$ plotted as χT versus temperature shown in Fig. 8a follows the predicted behaviour for a high-spin ground state upon subtraction of the spin-only contribution of $1.95\,cm^3\,mol^{-1}\,K$ from Cr^{3+} taken from the reference compound $[Fe(bpy)_3][LiCr(ox)_3]$. The contribution of the $[Co(bpy)_3]^{2+}$ complex to the total value of χT of $1.8\,cm^3\,mol^{-1}\,K$ at 10 K and $3.3\,cm^3\,mol^{-1}\,K$ at 300 K indicates that the trigonal crystal field splitting is comparatively small, but in order to determine the splitting quantitatively from the magnetic susceptibility measurements would require results with H parallel and perpendicular to the trigonal axis of the

complex. In the cubic crystal structure of the oxalate network this is not possible. EPR spectra (see below) will allow the determination of the trigonal splitting.

The behaviour of the analogous compound $[Co(bpy)_3][LiCr(ox)_3]$ in which the sodium on the oxalate backbone has been substituted by lithium is very different. At 10 K the contribution from $[Co(bpy)_3]^{2+}$ is only 0.40 $cm^3\ mol^{-1}$ K, indicating that at this temperature the low-spin state is the thermodynamically stable state. This in turn signifies that in the more confining cavity of the lithium analogue, the high-spin state is destabilised sufficiently for the low-spin state to become the ground state. However, the high-spin state is within thermal energies of the ground state, and as the temperature increases, the thermal population of the high-spin state results in a sigmoidal increase in χT. The fraction of complexes in the high-spin state can be calculated according to

$$\gamma_{HS} = \frac{(\chi T_{obs} - \chi T_{Cr^{3+}})/x - \chi T_{LS}}{\chi T_{HS} - \chi T_{LS}} \quad (9)$$

where χT_{HS} is taken from the curve measured for the high-spin compound, χT_{LS} is set equal to the value at 10 K, and for the neat compound the mole fraction of spin-crossover complexes $x = 1$. Fig. 9 shows the corresponding transition curve. At room temperature the high-spin fraction reaches a value of ~80%.

In addition to the pure compounds, Fig. 8a and b include χT curves for mixed crystals of composition $[M_{1-x}Co_x(bpy)_3][LiCr(ox)_3]$, M = Fe, Zn, and Fig. 9 includes the corresponding transition curves. For the former, the spin transition moves to higher temperatures and becomes more gradual, for the latter it moves to lower temperatures. As expected, the smaller $[Fe(bpy)_3]^{2+}$ complex enhances the "chemical" pressure effect, the larger $[Zn(bpy)_3]^{2+}$ complex reverses it to some extent. Furthermore, the more gradual curves for the mixed crystals with iron(II) as compared to the curve of the neat cobalt(II) compound indicate that cooperative effect are by no means negligible in this system.

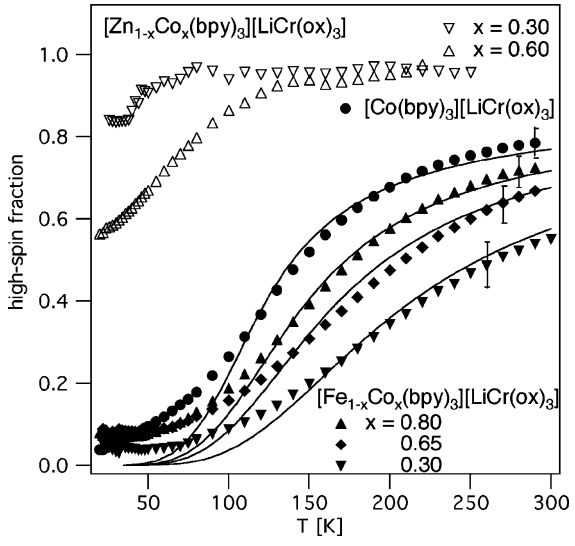

Fig. 9. Thermal spin transition curves for neat $[Co(bpy)_3][LiCr(ox)_3]$, $[Fe_{1-x}Co_x(bpy)_3][LiCr(ox)_3]$ and $[Zn_{1-x}Co_x(bpy)_3][LiCr(ox)_3]$. Solid lines: best fit according to the mean-field model (adapted from Ref. [19a]).

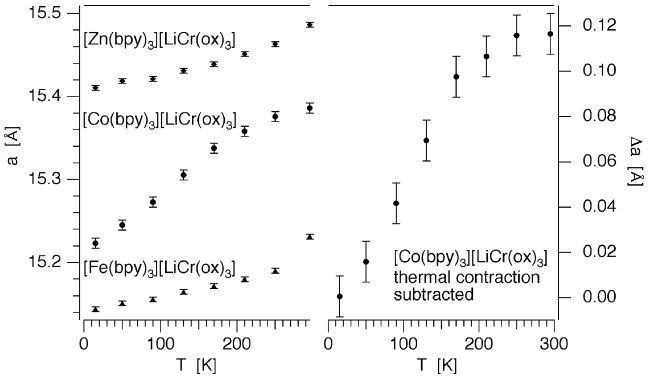

Fig. 10. The unit cell parameter a of $[M(bpy)_3][LiCr(ox)_3]$, M = Fe, Co, Zn, as a function of temperature (adapted from Ref. [19a]).

4.1.2. Structure

The oxalate networks of composition $[M(bpy)_3][M'M''(ox)_3]$ crystallise in the cubic and chiral spacegroup $P2_13$, $Z = 4$ [33]. For all tris-chelate complexes, that is for both $[M(bpy)_3]^{2+}$ as well as $[M''(ox)_3]^{3-}$, the point group symmetry is C_3. The four complexes of each type per unit cell are oriented along the three-fold axis of a tetrahedron. Apart from the unit cell parameter, the important structural parameters for the spin-crossover systems are the metal–ligand bond length, the bite and twist angles, and the dihedral angle of the bipyridine ligand. Fig. 10 shows the former as a function temperature for the spin-crossover system $[Co(bpy)_3][LiCr(ox)_3]$ and for the two reference systems $[M(bpy)_3][LiCr(ox)_3]$, M = Fe, Zn. Thus at 10 K, $a = 15.223$ Å and at 295 K $a = 15.386$ Å for $[Co(bpy)_3][LiCr(ox)_3]$. This corresponds to an increase of the unit cell volume of 115 Å or 29 $Å^3$ per complex, which comprises both the thermal expansion and the effect of the thermal spin transition. The results from the reference compounds show that the thermal expansion is responsible for about half of the total expansion. Considering that at room temperature the high-spin fraction is only around 80%, the actual volume difference between the high-spin and the low-spin state $\Delta V_{HL} \approx 18\ Å^3$ per complex. Table 1 shows the other important structural quantities for the spin-crossover system $[Co(bpy)_3][LiCr(ox)_3]$ and for the high-spin system $[Co(bpy)_3][NaCr(ox)_3]$. The most marked changes are observed for the Co–N bond lengths, with an estimate of $\Delta r_{HL} = 0.11$ Å. Other parameters such as the bite and the twist angle adapt to this difference.

4.1.3. Optical spectroscopy

The single crystal absorption spectrum of $[Co(bpy)_3][NaRh(ox)_3]$ shown in Fig. 11a with the band at 11,500 cm^{-1} typical for the spin-allowed $^4T_1 \rightarrow {}^4T_2$ ligand-field transition confirms the high-spin ground state of $[Co(bpy)_3]^{2+}$ in this compound. From it a value of the ligand-field parameter for the high-spin state of $10Dq^{HS} \approx 12{,}700\ cm^{-1}$ can be estimated.

Fig. 11b shows the single crystal absorption spectra as function of temperature in $[Co(bpy)_3][LiRh(ox)_3]$. The band in the NIR, present in the previous system, is no longer there. Instead there is a very broad band at 14,000 cm^{-1}. The intensity of this band decreases with increasing temperature. It

Table 1
Selected experimental and computational structural (Å, °) parameters for $[Co(bpy)_3]^{2+}$ in the high-spin (D_3 symmetry) and in the low-spin state (D_3 and C_2 symmetry)

	High-spin		Low-spin		
	Experimental[a]	Calculated[b]	Experimental[c]	Calculated[d] D_3	Calculated[d] C_2
Co–N	2.123	2.155	2.024	2.063	1.980/2.005, 2.243
C_2–C_2'	1.488	1.480	1.481	1.474	1.464/1.479
Bite angle	77.4	75.9	80.1	79.0	81.4/77.4
Twist angle	47.7	50.1	51.2	53.2	
Dihedral angle	0.5	4.5	0.1	6.4	3.5/5.3
Δr_{HL}[e]	0.099	0.092			

[a] $[Co(bpy)_3][NaCr(ox)_3]$ [19].
[b] DFT with the OLYP functional and the TZVP basis set implemented in ADF [32].
[c] $[Co(bpy)_3][LiCr(ox)_3]$ [19].
[d] One ligand on C_2, the other two connected by C_2.
[e] Averaged.

may be attributed to the spin-allowed set of ligand-field transitions $^2E \rightarrow {}^2T_2$, $^2T_1$ characteristic for the low-spin species. The corresponding ligand-field strength in the low-spin state $10Dq^{LS} \approx 15{,}500\,cm^{-1}$. According to the $1/r^n$ dependence of 10Dq with $n \approx 6$ for uncharged ligands, this allows an estimate

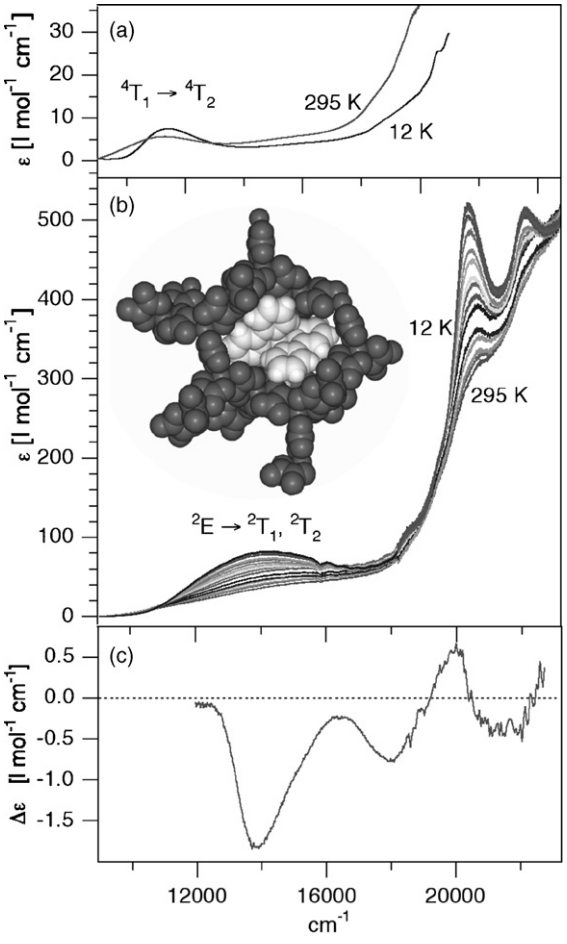

Fig. 11. (a) Single crystal absorption spectra of $[Co(bpy)_3][NaRh(ox)_3]$ at 12 and 295 K, (b) single crystal absorption spectra of $[Co(bpy)_3][LiRh(ox)_3]$ between 12 and 295 K, inset: model of the 3D oxalate network structure, and (c) single crystal CD spectrum of $[Co(bpy)_3][LiRh(ox)_3]$ at 4.2 K ((a) and (b) adapted from Ref. [19b]).

of the metal–ligand bond length difference of ~0.08 Å, which is in line with the crystallographic measurement.

The assignment of the higher energy bands of the low-spin species is less straightforward. They have been tentatively assigned to higher energy ligand-field transitions based on powder reflectivity measurements. The single crystal spectra of Fig. 11b give an extinction coefficient of more than 500 for the prominent band at 19,800 cm^{-1}, and with a half width of ~1000 cm^{-1} this is more likely to be a metal–ligand charge-transfer (MLCT) transition. This is corroborated by the CD spectrum shown in Fig. 11c. Whereas as the broad band at 14,000 cm^{-1} and the shoulder at 18,000 cm^{-1} carry a substantial CD signal, the more intense bands at higher energy only carry a very small signal in relation to their intensity. Indeed, TD-DFT calculations clearly identify the band structure at higher energies as metal–ligand charge transfer transitions [32].

4.1.4. EPR spectroscopy

EPR spectroscopy can give information on the axial ligand field. For the cubic crystal system of the oxalate network, it is quite intricate to extract $g_\parallel$ and $g_\perp$ with respect to the trigonal axis of the complex. Fig. 12 shows the single crystal EPR spectra in the X-band region of the doped system $[Zn_{1-x}Co_x(bpy)_3][LiRh(ox)_3]$, $x = 0.01$, at selected angles and at 4 K: (a) $H \perp$ to two out the four C_3 axis, (b) $H \parallel$ to one C_3 axis, (c) $H \parallel$ to one S_4 axis of the crystal. Basically the spectra show one or more strong signals at $g > 2$ with a strong angular dependence, and a weak almost isotropic signal with a clear hyperfine structure centred at g only slightly above 2. The former are due to high-spin the latter to low-spin cobalt(II).

The three spectra allow a quantitative determination of the trigonal splitting of the high-spin state. The low-field signal of spectrum (a) directly gives $g_\perp = 4.779$, and the high-field signal of spectrum (b) gives $g_\parallel = 2.774$. In spectrum (c) the orientation of all four complexes in the unit cell relative to the magnetic field is identical with an angle corresponding to 54.75°. The g-value of 4.206 is in line with the above values of $g_\parallel$ and $g_\perp$. Comparison with the curves of Fig. 6 results in a trigonal splitting of the high-spin state of $\Delta_{trig} = -300\,cm^{-1}$. In addition, the signals for the high-spin species are split, indicating a small rhombic distortion.

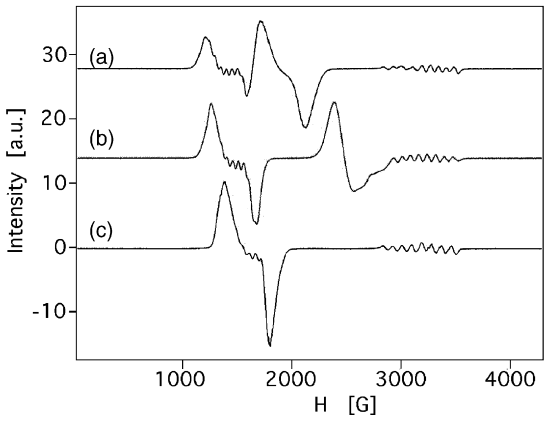

Fig. 12. EPR spectra of $[Zn_{1-x}Co_x(bpy)_3][LiRh(ox)_3]$, $x = 0.01$, at selected angles and at 4 K. (a) $H \perp$ to two out of the four C_3 axis, the angle between H and the other two complexes is 35.3°, (b) $H \parallel$ to one C_3 axis, the angle between H and the other three complexes is 70.5°, and (c) $H \parallel$ to one S_4 axis, all four complexes are equivalent with an angle of 54.75° between H and the molecular C_3 axis.

Indeed with Li as glue of the oxalate backbone, such a symmetry lowering has been documented before [34]. It is, however, small and probably disordered and therefore not observable by X-ray crystallography.

The low-spin species is present as a minority species. This is due to an inhomogeneous distribution of the zero-point energy difference as a result of which some of the complexes find themselves with a low-spin ground state. The observed signal shows a hyperfine splitting of $A = 170$ G in the form of eight lines due to the coupling to the $I = 7/2$ nucleus of cobalt. The g-value is almost isotropic varying from 2.074 to 2.155 as the angle is rotated. In trigonal symmetry one would expect a $g_\parallel$ value slightly larger than 2 due to second order spin–orbit coupling, and a $g_\perp$ value close to zero. The fact that g is almost isotropic and in the vicinity of 2 shows that the ^{2}E state is subject to a Jahn–Teller effect along an e vibration, that is, along the tetragonal distortion sketched in Fig. 7. Even though the crystal structure shows no indication of a symmetry lowering, this Jahn–Teller effect is not necessarily dynamic. Indeed, the micro-heterogeneity inherent in the crystal localises the system in one of the three formally equivalent potential minima.

4.1.5. Discussion of cobalt(II)-tris-2,2′-bipyridine

As mentioned in the introduction, DFT performs extremely well with respect to structure optimisation and frequency calculations. Table 1 compares the calculated structures of $[Co(bpy)_3]^{2+}$ in both spin states with the experimental values. Calculations were performed using the OLYP exchange-correlation functional and the high-quality TZP basis set as implemented in ADF [35]. Computational details may be found in Ref. [32]. For the high-spin state, the structure was optimised in D_3 point symmetry, for the low-spin state the structure was first optimised in D_3 and then allowed to relax to C_2. The agreement with experiment is very good indeed. In particular, the metal–ligand bond length difference between the high-spin and the low-spin state $\Delta r_{HL} = 0.1$ Å but also the other relevant structural parameters are well reproduced. The only angle that deviates substantially from experiment is the dihedral angle of the bpy ligand, but this is a comparatively floppy mode and its value is dictated by crystal packing. Whereas for the high-spin state, the geometry optimised in D_3 corresponds to a true minimum as verified by a frequency analysis, this is not the case for the low-spin state. The true minimum for the low-spin state has C_2 point symmetry with one ligand closer to the metal ion than the other two, the latter having two different Co–N bond lengths. This distortion is the result of the E × e Jahn–Teller effect. The calculated Jahn–Teller stabilisation energy is 1500 cm^{-1}, and the barrier height in the warped Mexican hat is 350 cm^{-1}. Thus DFT calculations corroborate and quantify the experimental results.

The experimental parameter of the trigonal ligand field for the ^{4}T$_1$ state is comparatively small and negative. Based on point charge arguments this would correspond to a geometric elongation of the coordination octahedron. However, in the tris-bipyridine complex the coordination octahedron is compressed. As has already been pointed out by Orgel, and as has been verified for tris-bipyridine complexes of other transition metal ions, tris-chelated complexes with conjugated ligands exert an effective trigonal ligand field, which destabilises the a_2 orbital. DFT calculations [32] take this into account and correctly predict a splitting of the ^{4}T$_1$ state with a ^{4}A$_2$ ground state. However, the predicted splitting between the trigonal components of the ^{4}T$_1$ state is 1800 cm^{-1}. This value is considerably larger than the experimentally derived value. This discrepancy could have two reasons: (a) the crystal packing strongly influences the trigonal splitting via the dihedral angle between the two pyridine moieties of bipyridine, (b) a pseudo Jahn–Teller effect in the ^{4}T$_1$ state influences the g values of the lowest energy Kramers doublet.

With due caution, the energies of all six Kramers doublets of the ^{4}T$_1$ state can be taken from Fig. 5 at $\Delta_{trig} = -300$ cm^{-1}. For the ^{2}E state, the Jahn–Teller effect replaces the electronic degeneracy of 4 by a vibronic degeneracy of 4. This determines the electronic partition functions in Eq. (5). Vibrational frequency calculations on the two spin states based on DFT can be used to calculate the vibrational partition functions. This leaves as only unknown parameters the zero-point energy difference ΔE°_{HL}, the lattice shift Δ_{lat} and the interaction constant Γ_{int}. Fig. 9 includes the calculated transition curves resulting from a simultaneous fit of Eq. (7) to the experimental curves for the different mole fractions of cobalt(II) in the series $[Fe_{1-x}Co_x(bpy)_3][LiRh(ox)_3]$, giving $\Delta E^\circ_{HL} = 310(9)$ cm^{-1}, $\Delta_{lat} = -225(9)$ cm^{-1}, and $\Gamma_{int} = 60(8)$ cm^{-1}. The fit is almost identical to the one given in Ref. [19], where Eq. (2) was used to express ΔG°_{HL}. In the latter ΔH°_{HL} and ΔS°_{HL} were used as fitting parameters instead of ΔE°_{HL}. The fact that at low temperatures the fit is not very satisfactory is due to an inhomogeneous distribution of the zero-point energy of some 100 cm^{-1}. The negative value of Δ_{lat} is in accordance with the more confining iron host lattice which destabilises the high-spin state of $[Co(bpy)_3]^{2+}$ and therefore pushes $T_{1/2}$ to higher temperatures. For the zinc host lattice Δ_{lat} is expected to be positive. The fact that for the very dilute system, the cobalt(II) complexes

are essentially in the high-spin state indicates that it must be slightly larger than the value of ΔE°_{HL}.

4.2. The cobalt(II)-bis-2,2′:6′,2″-terpyridine complex

As discussed in Section 2, the $[Co(terpy)_2]^{2+}$ was one of the first cobalt(II) spin-crossover complex reported in the literature. Already at an early stage it was noticed that the spin-crossover behaviour is complex and depends strongly on the second coordination sphere, that is, on the counterion and the nature and number of solvent molecules incorporated in the crystal lattice. The anhydrous $[Co(terpy)_2](ClO_4)_2$, for instance, is fully in the low-spin state at low temperatures and shows a transition to the high-spin state with a thermal population ~80% at room temperature [13]. The various hydrated forms, on the other hand, show different degrees of partial spin transitions with remnant high-spin fractions at low temperature, or temperature independent populations of the two spin states. In the following, the discussion is restricted to some well-defined systems, with no incorporation of solvent molecules.

4.2.1. Magnetic susceptibility

Fig. 13 shows the magnetic susceptibility plotted as the product χT versus temperature for the neat compounds $[Co(terpy)_2](ClO_4)_2$ and $[Co(terpy)_2](PF_6)_2$, and for mixed crystals of composition $[Fe_{1-x}Co_x(terpy)_2](PF_6)_2$ and $[Zn_{1-x}Co_x(terpy)_2](PF_6)_2$, with $x = 0.17$ and 0.12, respectively. The curve for $[Co(terpy)_2](ClO_4)_2$ is in perfect agreement with literature [13] and shows the typical behaviour for a spin transition of cobalt(II) with a low-temperature value of χT of 0.4 $cm^3\,mol^{-1}\,K$ corresponding to the spin-only value of the low-spin state and the thermal population of the high-spin state of around 80% at room temperature. However, knowing that even though the transition is gradual, cooperative effects are still non-negligible, a fit using Eqs. (1) and (2) is not advisable, and in the absence of any reference data on dilute systems, an analysis according to Eq. (7) is not possible. Unfortunately, the curves from the mixed systems cannot be used as reference data. The iron(II) host destabilises the high-spin state to such an extent that the population of the high-spin state only very gradually sets in towards room temperature, and in the zinc(II) host the $[Co(terpy)_2]^{2+}$ complex is essentially in the high-spin state at all temperatures. Likewise in neat $[Co(terpy)_2](PF_6)_2$, the cobalt(II) complex is essentially in the high-spin state. Qualitative comparison of the experimental curve with the calculated curves of Fig. 3b indicates that there is a comparatively strong tetragonal field corresponding to a compression of the octahedron and therefore a ^4E ground state. However, the dip in the experimental curve above 100 K cannot be reproduced within the model of a tetragonal ligand field. This dip constitutes a first indication that for this compound the high-spin state is the ground state but that a component of the low-spin state lies energetically between the two lowest energy Kramers doublets of the high-spin state. As a result, the low-spin state may become partially populated at higher temperatures. Proof based on optical spectra of this will be provided below.

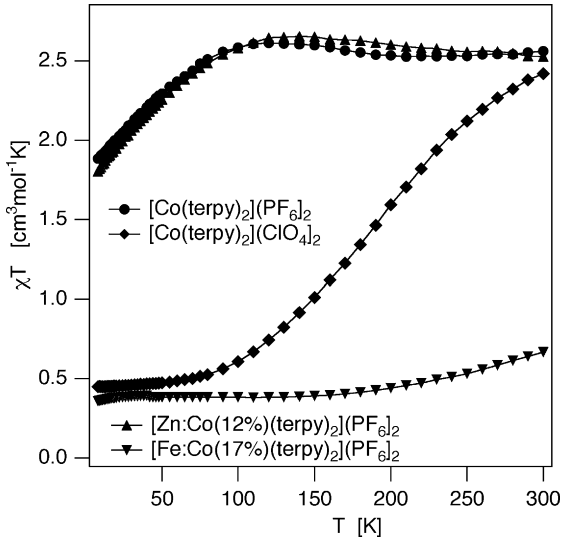

Fig. 13. The product χT as function of temperature for $[Co(terpy)_2](ClO_4)_2$ (♦), $[Co(terpy)_2](PF_6)_2$ (●), and the mixed systems $[Fe_{1-x}Co_x(terpy)_2](PF_6)_2$, $x = 0.17$ (▼) and $[Zn_{1-x}Co_x(terpy)_2](PF_6)_2$, $x = 0.12$ (▼). For the latter two χT is given per mole of cobalt(II).

4.2.2. Optical spectroscopy

Fig. 14 shows the absorption spectrum of $[Co(terpy)_2]^{2+}$ as a function of temperature in a mixture of acetonitrile and proprionitrile. The comparatively intense band structure with peaks at 18,000, 20,000, and 22,500 cm^{-1}, which is typical for the MLCT transition of the low-spin species and which decreases in intensity with increasing temperature shows that for this complex in solution a thermal spin transition occurs. In methanol the simple thermodynamic analysis of the data using Eqs. (1) and (2) by Beattie et al. [36] yields values for ΔH°_{HL} and ΔS°_{HL} of 774 cm^{-1} and 2.21 $cm^{-1}\,K^{-1}$, respectively, and for $T_{1/2}$ of 329 K. The spectra in Fig. 14 are qualitatively in accordance with these values, however in the mixture of acetonitrile and proprionitrile $T_{1/2}$ is slightly lower.

Fig. 14 includes the single crystal absorption spectrum of $[Co(terpy)_2](ClO_4)_2$. Similar to $[Co(bpy)_3]^{2+}$ in the oxalate net-

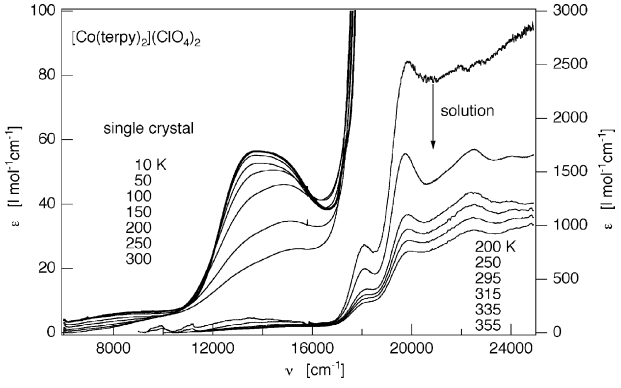

Fig. 14. Single crystal absorption spectrum of $[Co(terpy)_2](ClO_4)_2$ (left hand side), and solution spectrum of $[Co(terpy)_2]^{2+}$ in a mixture of acetonitrile/proprionitrile (right hand side) as function temperature.

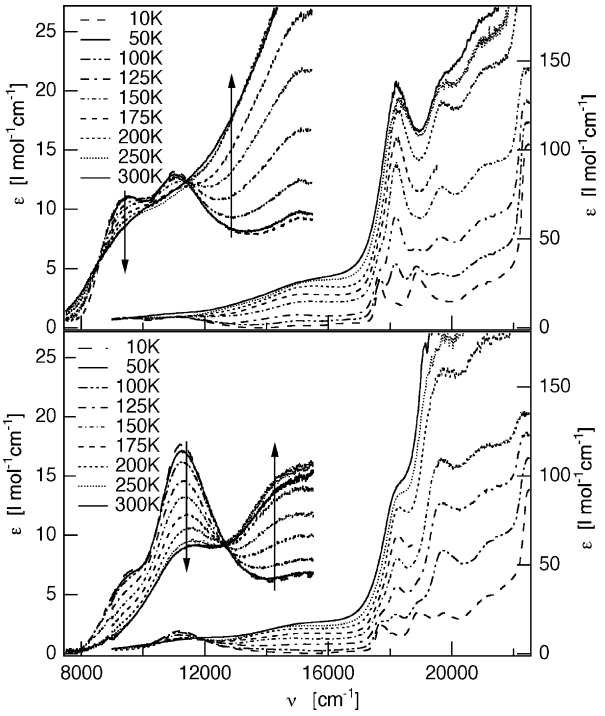

Fig. 15. Polarised single crystal absorption spectra of $[Co(terpy)_2](PF_6)_2$ as a function temperature with *E* parallel (top) and perpendicular (bottom) the long axis of crystal.

work it shows an asymmetric absorption band with an intensity typical for spin-allowed d–d transitions, which may likewise be attributed to the $^2E \rightarrow {}^2T_2, {}^2T_1$ transition characteristic for the low-spin species. The intensity of this band plotted as a function of temperature directly gives a spin transition curve, which is in perfect agreement with the one derived from magnetic susceptibility measurements [13]. An additional band centred at 7500 cm^{-1} has been attributed to the intra-configurational ^2E transition in the strong axial ligand field [9] due to the large difference between axial and equatorial Co–N bond lengths in the low-spin state.

Fig. 15 shows the single crystal absorption spectra of $[Co(terpy)_2](PF_6)_2$ as a function of temperature in two polarisation directions. They are strikingly different compared to the one of the perchlorate. According to the magnetic susceptibility measurements, the $[Co(terpy)_2]^{2+}$ complex is essentially in the high-spin state at all temperatures. It is therefore straightforward to assign the split band with components at 9200 and 11,600 cm^{-1}, respectively, to the transitions from the $^4T_1$ ground state to the tetragonal components of the $^4T_2$ state. As is usual for d–d bands, they broaden out somewhat with increasing temperature. However, the overall temperature dependence of the spectrum is very different from the temperature dependence observed for high-spin $[Co(bpy)_2]^{2+}$ in $[Co(bpy)_3][NaRh(ox)_3]$. The marked increase in intensity observed in the region of the low-spin MLCT transition, that is, for the peaks at 18,000, 20,000 and 22,000 cm^{-1}, indicates a most unusual partial thermal population of the low-spin state. Comparison of the intensity of the three bands with the solution spectrum indicates that the maximum population of the low-spin state is approximately 6%. Likewise

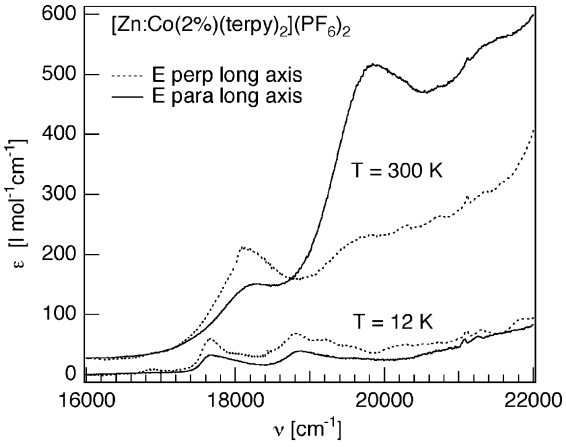

Fig. 16. Single crystal absorption spectra of $[Zn_{1-x}Co_x(terpy)_2](PF_6)_2$, $x = 0.02$, at 12 and at 300 K. The increasing intensity of the bands at 18,000 and 20,000 cm^{-1} indicate a partial population of the low-spin state at elevated temperatures.

the broad and unstructured band appearing at 15,000 cm^{-1} can be attributed to the low-spin $^2E \rightarrow {}^2T_1$, $^2T_2$ d–d transitions. In the dilute mixed crystal system $[Zn_{1-x}Co_x(terpy)_2](PF_6)_2$, $x = 0.02$, the behaviour is quite similar. Although at this concentration of the cobalt complex, the d–d transitions are too weak to be discernible, the temperature dependent spectra shown in Fig. 16, clearly show a thermal population of the low-spin state of almost 10% at room temperature. Thus optical spectra support the tentative conclusion from the magnetic susceptibility measurements.

4.2.3. EPR spectra

A discussion of the thermal spin transition in $[Co(terpy)_2](ClO_4)_2$ and the anomalous behaviour of $[Co(terpy)_2](PF_6)_2$ and the dilute system $[Zn_{1-x}Co_x(terpy)_2](PF_6)_2$ necessitates a detailed understanding of the electronic structure of the two spin states. This may be provided by the powder EPR spectra (X-band) shown in Fig. 17a and b of the dilute systems $[Zn_{1-x}Co_x(terpy)_2](PF_6)_2$, $x = 2\%$, and $[Fe_{1-x}Co_x(terpy)_2](PF_6)_2$, $x = 4\%$, at 4.2 K. The spectrum of the latter only shows a strong signal with hyperfine structure at around $g = 2$, which is typical for low-spin cobalt(II) in agreement with the magnetic susceptibility measurements. A simulation of the experimental spectrum indicates that in addition to the tetragonal ligand field inherent to the $[Co(terpy)_2]^{2+}$ complex, there is a weak rhombic distortion probably due to crystal packing, with $g_z = 2.19$, $g_x = 2.09$, and $g_y = 2.08$, and hyperfine coupling constants $A_{xx} = 0.0056\ cm^{-1}$, $A_{yy} = 0.0054\ cm^{-1}$, and $A_z = 0.0095\ cm^{-1}$. The spectrum of the former is dominated by two signals centred at 1000 and 2500 G, which are typical for high-spin cobalt(II) in a lower symmetry environment. Simulation of the spectrum yields $g_z = 6.80$, $g_x = 2.98$, and $g_y = 2.70$, and anisotropic hyperfine coupling constants with $A_{zz} = 0.030\ cm^{-1}$ and $A_{xx} \approx A_{yy} = 0.0050\ cm^{-1}$. Setting $g_\parallel = g_z$ and $g_\perp = (g_x + g_y)/2 = 2.79$ for D_{2d} symmetry, allows an estimate of the tetragonal splitting using Fig. 6. As expected for a tetragonally compressed octahedron Δ_{tetr} is positive and takes on a value of 600 cm^{-1}. This value is still comparatively small

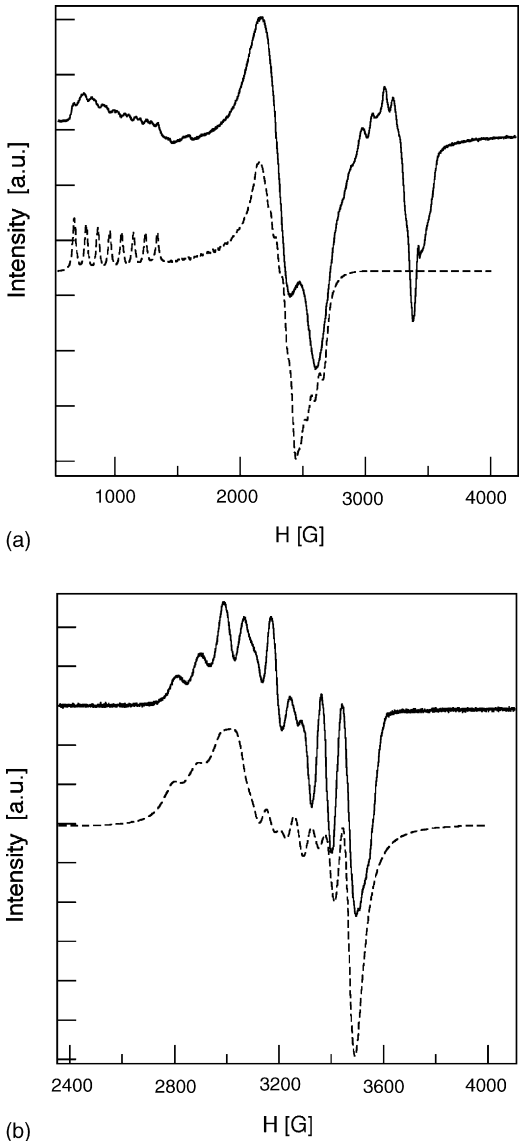

Fig. 17. Powder EPR spectra of (a) $[Zn_{1-x}Co_x(terpy)_2](PF_6)_2$, $x = 0.02$, and (b) $[Fe_{1-x}Co_x(terpy)_2](PF_6)_2$, $x = 0.04$, at 4.2 K, X-band, experimental (full lines), simulations (broken lines).

and reflects the smaller difference in equatorial and axial Co–N bond lengths in the high-spin state as compared to the low-spin state. All values given above are in agreement with the values given in Ref. [9] for $[Co(terpy)_2]^{2+}$ in a number of different environments.

In addition to the transitions of the high-spin species, the powder spectrum with the zinc host shows a low-spin signal around $g = 2$. The band is much weaker than the high-spin signals, and taking into account that low-spin signals are often more intense than high-spin signals, this corresponds to a minority species. It is probably due to an inhomogeneous distribution of the zero-point energy difference between the high-spin and the low-spin manifolds such that a minority of complexes has a low-spin ground state. Inhomogeneous broadening very much depends on sample preparation. It is usually much larger in powder samples, and indeed, the doped single crystal used for the optical measurements and for preliminary single crystal EPR measurements suffers less from such broadening as there is no indication of an appreciable low-spin population at low temperatures.

4.2.4. Discussion of cobalt(II)-bis-2,2′:6′,2″-terpyridine

As expected, the chemical environment modulates the zero-point energy difference. Thus the more compact structure of the perchlorate as compared to the hexafluorophosphate turns the essentially high-spin compound $[Co(terpy)_2](PF_6)_2$ into the spin-crossover compound $[Co(terpy)_2](ClO_4)_2$. Likewise, in the dilute mixed crystal $[Fe_{1-x}Co_x(terpy)_2](PF_6)_2$, $x = 0.04$, the more compact structure of the host lattice destabilises the high-spin state. The most striking observation, however, is the thermal population of the low-spin state in $[Co(terpy)_2](PF_6)_2$. In iron(II) such a behaviour is not possible, because the entropic term always favours the high-spin state to such an extent that if it is the actual ground state, the population of the low-spin state remains negligible at all temperatures. In cobalt(II) systems the change in vibrational frequencies is much smaller than in iron(II) systems, therefore the vibrational contribution to ΔS°_{HL} is typically only around $1.5\,cm^{-1}\,K^{-1}$. If at the same time the multiplet splitting of the high-spin state is large enough, then a component of the low-spin state can lie between the ground state Kramers doublet and the first excited Kramers doublet of the high-spin state. Thus with $\Delta S^{vib}_{HL} \approx 1.5\,cm^{-1}\,K^{-1}$ and taking the electronic energy levels of the high-spin state from Fig. 5 at $\Delta_{tetr} = 600\,cm^{-1}$, the 5–10% low-spin fraction appearing at $T > 100$ K indicates that the lower energy component of the low-spin state is $\sim 100\,cm^{-1}$ above the lowest energy component of the high-spin state.

5. Conclusions

The two complexes discussed in the above case studies allow for an in depth understanding of some of the more important aspects of spin-crossover in cobalt(II) complexes. The detailed investigation of cobalt(II) spin-crossover systems requires a combination of a number of different experimental techniques, and the theoretical description of the electronic structure as well as the spin transition is more complex than for iron(II) spin-crossover systems. As a result of the smaller ratio of electronic degeneracies and smaller differences in vibrational frequencies between the two spin states, the range of ligand-field strengths for which spin transitions can be expected is smaller. Therefore the number of known cobalt(II) spin-crossover complexes is rather low, and the influence of the environment, that is, anion, solvent or host dependence, is much more subtle. Most spin transitions are gradual, and high-spin fractions above 80% are rarely reached. Elastic interactions are usually less important. Nevertheless, symmetry lowering due to a strong Jahn–Teller effect in the low-spin state can lead to cooperative phenomena in some cases.

Even though values for the thermodynamic parameters ΔH°_{HL} and ΔS°_{HL} as derived from a fit of the experimental data using Eqs. (1)–(3) may be found in the literature, they should be viewed with caution, as their physical significance is limited. Rather, for a correct description of the thermal spin transition,

the multiplet splittings and therefore the effective temperature dependence of the thermodynamic parameters have to be taken into account explicitly.

In contrast to iron(II) spin-crossover systems, for which the high-spin → low-spin relaxation has been studied in great detail making use of the photo-physical population of the high-spin state [37], there is only a single report of a room temperature estimate of a high-spin → low-spin relaxation rate constant in the literature [36]. With an upper limit of $5 \times 10^8\ s^{-1}$, the rate constant is several orders of magnitude larger than for comparable iron(II) spin-crossover systems. This is basically due to the smaller energy barrier between the two states as a result of the smaller bond length difference. It would be interesting to actually determine the temperature dependence of the high-spin → low-spin relaxation down to liquid helium temperatures, but this is hampered by the fact that the photo-physical population of the high-spin state is not very efficient for cobalt(II) complexes.

Acknowledgements

We thank the Swiss National Science Foundation for financial support, the "Centro Svizzero di Calcolo Scientifico" for computational resources, and the EU for financial support within the NoE "Magmanet" (Contract Nr. NMP3-CT-2005-515767-2).

References

[1] (a) L. Cambi, L. Szego, A. Cagnasso, Atti accad Lincei 13 (1931) 168;
(b) L. Cambi, L. Szego, Atti accad Lincei 15 (1931) 329;
(c) L. Cambi, L. Szego, Atti accad Lincei 15 (1932) 599.
[2] R.C. Stoufer, D.H. Busch, W.B. Hadley, J. Am. Chem. Soc. 83 (1961) 3732.
[3] K. Madeja, E. König, Inorg. Nucl. Chem. 25 (1963) 377.
[4] (a) H. Spiering, Top. Curr. Chem. 235 (2004) 171;
(b) H. Spiering, K. Boukheddaden, J. Linares, F. Varret, Phys. Rev. B 70 (2004) 184;
(c) H. Spiering, E. Meissner, H. Köppen, E.W. Müller, P. Gütlich, Chem. Phys. 68 (1982) 65.
[5] (a) M.A. Hoselton, L.J. Wilson, R.S. Drago, J. Am. Chem. Soc. 97 (1975) 1722;
(b) B.A. Katz, C.E. Strouse, J. Am. Chem. Soc. 101 (1979) 6214;
(c) M. Mikami, Konno, Y. Saito, Acta Crystallogr. B38 (1982) 452;
(d) E.A. Binstead, J.K. Beattie, Inorg. Chem. 25 (1986) 1481;
(f) J.F. Létard, P. Guionneau, L. Rabardel, J.A.K. Howard, A.E. Goeta, D. Chasseau, O. Kahn, Inorg. Chem. 37 (1998) 4432;
(h) P. van Koningsbruggen, Y. Garcia, O. Kahn, L. Fournes, H. Kooijman, A.L. Spek, J.G. Haasnoot, J. Moscovici, K. Provost, A. Michalowicz, F. Renz, P. Gütlich, Inorg. Chem. 39 (2000) 1891;
(i) D. Chernyshov, M. Hostettler, K.W. Törnroos, H.-B. Bürgi, Angew. Chem. Int. Ed. 42 (2003) 3825.
[6] (a) H. Oshio, K. Toriumi, Y. Maeda, Y. Takashima, Inorg. Chem. 30 (1991) 4252;
(b) Y. Maeda, H. Oshio, K. Toriumi, Y. Takashima, J. Chem. Soc. Dalton Trans. (1991) 1227;
(c) Y. Nishida, K. Kino, S. Kida, J. Chem. Soc. Dalton Trans. (1987);
(d) Y. Maeda, H. Oshio, Y. Tanigawa, T. Oniki, Y. Takashima, Bull. Chem. Soc. Jpn. 64 (1991) 1522;
(e) S. Floquet, A.J. Simaan, E. Rivière, M. Nierlich, P. Thuéry, J. Ensling, P. Gütlich, J.-J. Girerd, M.-L. Boillot, Dalton. Trans. (2005) 1734;
(f) A.J. Simaan, M.-L. Boillot, R. Carrasco, J. Cano, J.-J. Girerd, T.A. Mattioli, J. Ensling, H. Spiering, P. Gütlich, Chem. Eur. J. 11 (2005) 1779.
[7] (a) P. Charpin, M. Nierlich, D. Vigner, M. Lance, P. Thuery, J. Zarembowitch, F. D'Yvoire, J. Crystallogr. Spectrosc. Res. 18 (1988) 429;
(b) P. Thuery, J. Zarembowitch, A. Michailowicz, O. Kahn, Inorg. Chem. 26 (1987) 851.
[8] R. Sieber, S. Decurtins, H. Stoeckli, C. Evans, D. Wilson, J.A.K. Yufit, S.C. Howard, A. Capelli, Hauser, Chem. Eur. J. 6 (2000) 361.
[9] S. Kremer, W. Henke, D. Reinen, Inorg. Chem. 21 (1982) 3013.
[10] P. Gütlich, H.A. Goodwin (Eds.), Spin Crossover in Transition Metal Complexes, vols. I–III, Springer, Heidelberg, Top. Curr. Chem., 233–235, 2004.
[11] J. Zarembowitch, New J. Chem. 16 (1992) 255.
[12] H.A. Goodwin, Top. Curr. Chem. 234 (2004) 23.
[13] (a) R. Hogg, R.G. Wilkins, J. Chem. Soc. (1962) 341;
(b) J.S. Judge, W.A. Baker, Inorg. Chim. Acta 1 (1967) 68.
[14] B.N. Figgis, E.S. Kucharski, A.H. White, Aust. J. Chem. 36 (1983) 1537.
[15] A.B. Gaspar, C.M. Munoz, V. Niel, J.A. Real, Inorg. Chem. 40 (2001) 9.
[16] (a) B.J. Childs, D.C. Craig, M.L. Scudder, H.A. Goodwin, Inorg. Chim. Acta 274 (1998) 32;
(b) E.C. Constable, T. Kulke, M. Neuburg, M. Zehnder, New J. Chem. 21 (1997) 1091.
[17] (a) A.B.P. Lever, Inorganic Electronic Spectroscopy, 2nd ed., Amsterdam, Elsevier, 1984, p. 421ff;
(b) R.A. Palmer, T.S. Piper, Inorg. Chem. 5 (1966) 864.
[18] (a) K. Mizuno, J.H. Lunsford, Inorg. Chem. 22 (1983) 3484;
(b) S.K. Tiwary, S. Vasudevan, Chem. Phys. Lett. 277 (1997) 84;
(c) S.K. Tiwary, S. Vasudevan, Inorg. Chem. 37 (1998) 5239.
[19] (a) M. Zerara, A. Hauser, Chem. Phys. Chem. 5 (2004) 395;
(b) A. Hauser, N. Amstutz, S. Delahaye, S. Schenker, A. Sadki, R. Sieber, M. Zerara, Struct. Bond. 106 (2004) 81.
[20] D. Ongo, A.D. Rae, H.A. Goodwin, Inorg. Chim. Acta 178 (1990) 151.
[21] (a) J. Zarembowitch, O. Kahn, Inorg. Chem. 23 (1984) 589;
(b) C. Roux, J. Zarembowitch, J.P. Itie, M. Verdaguer, E. Dartyge, A. Fontaine, H. Tolentino, Inorg. Chem. 30 (1991) 3174;
(c) S.G. Sreerama, D. Shyamraj, S. Pal, S. Pal, Indian J. Chem. 42A (2003) 2352.
[22] (a) J.B. Kennedy, G.D. Fallon, M.K.C. Bryan, K.S. Murray, Inorg. Chem. 23 (1984) 580;
(b) F. Tuna, L. Patron, E. Rivière, M.-L. Boillot, Polyhedron 19 (2000) 1643;
(c) A. Nivorozhkin, H. Toftlund, M. Nielsen, J. Chem. Soc. Dalton (1994) 361.
[23] S. Sugano, Y. Tanabe, H. Kamimura, Multiplets of Transition Metal Ions Pure and Applied Physics, vol. 33, Academic Press, New York, 1970.
[24] (a) A.H. Ewald, R.L. Martin, A.H. White, Proc. Roy. Soc. A 280 (1964) 235;
(b) E. König, Berichte der Bunsengesellschaft für Phys Chem. 76 (1972) 975.
[25] F.E. Mabbs, D.J. Machin, Magnetism and Transition Metal Complexes, Chapmann & Hall, London, 1973.
[26] (a) L.E. Orgel, J. Chem. Soc. (1961) 3683;
(b) A. Ceulemans, M. Dendooven, L.G. Vanquickenborne, Inorg. Chem. 24 (1985) 1153.
[27] (a) B.N. Figgis, M.A. Hitchmann, Ligand Field Theory and its Applications, Wiley–VCH, New York, 2000;
(b) I.B. Bersuker, The Jahn–Teller Effect and Vibronic Interactions in Modern Chemistry, Plenum Press, New York, 1984.
[28] W. Koch, M.C. Holthausen, A Chemist's Guide to Density Functional Theory, Wiley-VCH, New York, 2000.
[29] (a) H. Paulsen, A.X. Trautwein, Top. Curr. Chem. 235 (2004);
(b) M.L. Lawson Daku, A. Vargas, A. Hauser, A. Fouqueau, M.E. Casida, Chem. Phys. Chem. 6 (2005) 1393;
(c) O. Salomon, M. Reiher, B.A. Hess, J. Chem. Phys. 117 (2002) 4737.
[30] P. Adler, H. Spiering, P. Gütlich, Inorg. Chem. 26 (1987) 3840.
[31] C.G. Barraclough, Faraday Trans. 62 (1966) 1033.

[32] A. Vargas, M. Zerara, E. Krausz, A. Hauser, M. Lawson, J. Chem. Theory Comput., in press.
[33] (a) S. Decurtins, H.W. Schmalle, P. Schneuwly, J. Ensling, P. Gütlich, J. Am. Chem. Soc. 116 (1994) 9521;
(b) S. Decurtins, H.W. Schmalle, R. Pellaux, P. Schneuwly, A. Hauser, Inorg. Chem. 35 (1996) 1451.
[34] M.E. von Arx, A. Hauser, J. Phys. Chem. A 106 (2002) 7106.
[35] Amsterdam Density Functional program, Release ADF2004.01, Theoretical Chemistry, Vrije Universiteit Amsterdam, The Netherlands, http://www.scm.com.in.
[36] (a) J.K. Beattie, R.A. Binstead, M.T. Kelso, P. Del Favero, T.G. Dewey, D.H. Turner, Inorg. Chim. Acta 235 (1995) 245;
(b) J.K. Beattie, Adv. Inorg. Chem. 32 (1988) 1.
[37] A. Hauser, Top. Curr. Chem. 234 (2004) 155.